N-doped carbon shell encapsulated PtZn intermetallic nanoparticles as highly efficient catalysts for fuel cells

Yakun Xue[1], Huiqi Li[1], Xieweiyi Ye[1], Shuangli Yang[1], Zhiping Zheng[1], Xiao Han[1], Xibo Zhang[1], Luning Chen[1], Zhaoxiong Xie[1,2], Qin Kuang[1] (✉), and Lansun Zheng[1]

[1] State Key Laboratory of Physical Chemistry of Solid Surfaces & Department of Chemistry, College of Chemistry and Chemical Engineering, Xiamen University, Xiamen 361005, China
[2] Pen-Tung Sah Institute of Micro-Nano Science and Technology, Xiamen University, Xiamen 361005, China

ABSTRACT

The high cost and poor durability of Pt nanoparticles (NPs) have always been great challenges to the commercialization of proton exchange membrane fuel cells (PEMFCs). Pt-based intermetallic NPs with a highly ordered structure are considered as promising catalysts for PEMFCs due to their high catalytic activity and stability. Here, we reported a facile method to synthesize N-doped carbon encapsulated PtZn intermetallic (PtZn@NC) NPs via the pyrolysis of Pt@Zn-based zeolitic imidazolate framework-8 (Pt@ZIF-8) composites. The catalyst obtained at 800 °C (10%-PtZn@NC-800) was found to exhibit a half-wave potential ($E_{1/2}$) up to 0.912 V versus reversible hydrogen electrode (RHE) for the cathodic oxygen reduction reaction in an acidic medium, which shifted by 26 mV positively compared to the benchmark Pt/C catalyst. Besides, the mass activity and specific activity of 10%-PtZn@NC-800 at 0.9 V versus RHE were nearly 3 and 5 times as great as that of commercial Pt/C, respectively. It is worth noting that the PtZn@NC showed excellent stability in oxygen reduction reaction (ORR) with just 1 mV of the $E_{1/2}$ loss after 5,000 cycles, which is superior to that of most reported PtM catalysts (especially those disordered solid solutions). Furthermore, such N-doped carbon shell encapsulated PtZn intermetallic NPs showed significantly enhanced performances towards the anodic oxidation reaction of organic small molecules (such as methanol and formic acid). The synergistic effects of the N doped carbon encapsulation structure and intermetallic NPs are responsible for outstanding performances of the catalysts. This work provides us a new engineering strategy to acquire highly active and stable multifunctional catalysts for PEMFCs.

KEYWORDS

intermetallic nanoparticles, oxygen reduction reaction, N-doping, metal-organic frameworks, pyrolysis

1 Introduction

Proton exchange membrane fuel cells (PEMFCs) as energy source device with promising sustainable energy conversion technology have attracted more and more attentions [1–3]. To date, Pt-based catalysts with high catalytic activity are considered as the best catalyst for both the anodic oxidation reaction (methanol, formic acid and molecular hydrogen) and cathodic oxygen reduction reaction (ORR) in the PEMFCs [4–9]. However, the application of Pt catalysts is greatly limited because of the high cost, slow kinetics and poor stability over long-term reaction. Recently, alloying Pt with 3d transition metals M (M refers to transition metals such as Fe, Ni, Co, Cu, Zn, etc.) has proven an efficiency strategy to improve the performance of Pt-based catalysts towards PEMFCs [10–17]. However, the PtM alloys generally form as disordered solid solutions, which often suffer from the leaching of transition metal M under electrochemical conditions, thereby resulting in the decay of catalytic activity [18]. Of note, intermetallic nanoparticles (NPs), another form of alloy with a ordered occupancy of Pt and M atoms, are often found to exhibit significantly enhanced activity, anti-toxicity as well as stability compared to those disordered solid solutions when acting as fuel cell catalysts [7, 8, 19–21].

Wrapping active metal NPs with a carbon layer of a proper thickness is another effective strategy to improve the catalyst activity and stability in many electrocatalytic processes including ORR [22–27]. The unique carbon encapsulation structure can not only greatly improve the catalysts' ability of activating oxygen, but also protect the active metal components (such as transition metals) in catalysts from the leaching under harsh catalytic conditions (e.g., strong acidity or alkalinity) [28–30]. Moreover, many studies revealed that doping with p-block elements (especially N doping) can effectively modify the electronic structure of carbon-based materials, thereby facilitating ORR on carbon supported catalysts [31–33]. Based on these successes, the hybrid structure with PtM intermetallic NPs encapsulated in N-doped carbon is supposed to be an ideal architecture of catalysts with high activity and high stability in electrocatalysis processes [32, 33]. But the biggest current challenge is how to fabricate such complicated architectural catalysts simply and efficiently.

Recently, metal-organic frameworks (MOFs) have proven to be a kind of promising precursors for the synthesis of heteroatom-doped carbon supported electro-catalysts through thermal decomposition due to its highly ordered porous structure, large specific surface area and uniform distribution of hetero-atoms [34–37]. In this study, we successfully synthesized N-doped carbon (NC) shell encapsulated intermetallic PtZn (PtZn@NC) NPs via the pyrolysis of Pt@MOF composites with Pt NPs incorporated in Zn-based zeolitic imidazolate framework-8 (ZIF-8) under H₂/Ar atmosphere. In this synthetic route, the PtZn intermetallic nanoparticles (NPs) were *in situ* generated

Address correspondence to qkuang@xmu.edu.cn

via alloying Pt with Zn reduced from ZIF-8 and embedded in as-formed N-doped carbon during the pyrolysis process of precursors. Strikingly, the resulting PtZn@NC catalyst obtained at 800 °C not only exhibited significantly improved catalytic activity and stability for the cathodic ORR in an acidic medium, but also exhibited excellent properties in anodic oxidation reaction of small organic molecules such as formic acid and methanol.

2   Experiment

Chloroplatinic acid ($H_2PtCl_6 \cdot 6H_2O$), zinc nitrate hexahydrate (Zn $(NO_3)_2 \cdot 6H_2O$), polyvinylpyrrolidone (PVP, K-30), methanol and ethanol were analytical reagents and purchased from Sinopharm Chemical Reagent Co. Ltd. (Shanghai, China). 2-methylimidazole were analytical reagents and purchased from J.K. All reagents were used as received without further purification.

2.1   Synthesis of 5 nm PVP capped Pt NPs

According to literature [38], 133 mg PVP, 180 mL methanol and 15.5 mL aqueous solution of H_2PtCl_6 (77.23 mM) were mixed and refluxed at 60 °C in a 500 mL flask for 3 h under air. After removing methanol with rotary evaporator, Pt NPs were precipitated by acetone and methanol (7:3) several times and centrifuged at 10,000 rpm for 8 min. Then, the sample was dispersed with methanol (5 mg/mL).

2.2   Synthesis of rhombic dodecahedral Pt@ZIF-8 with different Pt contents

In the typical synthetic process, 40 mL 2-methylimidazole (2-Mim, 5.5 g) methanol solution, 3 mL $Zn(NO_3)_2 \cdot 6H_2O$ (0.464 g) methanol solution, and 7.16 mL PVP capped Pt NPs stock solution were successively added in a 100 mL blue cover bottle. Then, the mixture was stirred for 6 h at room temperature. The sample was precipitated by ethanol three times and dried in a vacuum dryer at 60 °C for 24 h. The theoretical Pt content in the Pt@ZIF-8 precursor was calculated to be ca. 10 wt.% according to the raw ratio of Pt NPs relative to ZIF-8. To obtain Pt@ZIF-8 with 1 wt.%, 2 wt.%, 5 wt.%, 15 wt.%, and 20 wt.% Pt contents, the amounts of the PVP capped Pt NPs stock solution added were changed to 0.715, 1.43, 3.58, 12.615, and 17.875 mL, respectively. For convenience, the resulting precursors were denoted as W%-Pt@ZIF-8 (W = 1, 2, 5, 10, 15, 20) according to the theoretical Pt contents.

2.3   Synthesis of intermetallic PtZn@NC hybrid catalysts

In a typical synthesis process, 50 mg 10%-Pt@ZIF-8 precursors were moved into a quartz boat and placed in a tube furnace. The pyrolysis was heated at 200 °C for 1 h to remove guest molecules in MOF cavities and then calcined at given higher temperature (600, 700, 800, 1,000 °C) under a 600 mL/min flow of 5% H_2/Ar for 5 h and with a ramping rate of 5 °C/min. For convenience, the resulting final products were denoted as 10%-PtZn@NC-X (X = 600, 700, 800, 1,000) according to the pyrolysis temperatures.

2.4   Characterization of samples

The morphology and crystal structure of samples were observed by a scanning electron microscope (SEM, Hitachi S4800) equipped with energy dispersive X-ray (EDX) spectroscopy and transmission electron microscope (TEM, JEOL2100) with an accelerating voltage of 200 kV. The composition of samples was determined by power X-ray diffraction (XRD) on Rigaku Ultima IV diffractometer (Cu Kα radiation, 40 kV, 30 mA). The high-angle annular dark-field scanning transmission electron microscopy (HAADF-STEM) and EDX spectroscopy were performed with an FEI TECNAI F30 microscope operated at 300 kV. Inductively coupled plasma mass spectrometry (ICP-MS) and Varioel EL III elemental analyzer were applied to

determine the actual metal content. Before the ICP-MS analysis, the samples were digested with mixture of HCl and HNO_3 (3:1, volume ratio). X-ray photoelectron spectroscopy (XPS) measurements were performed on an ESCALab 250 X-ray photoelectron spectrometer, using non-monochromatic Al Kα X-ray as the excitation source. The XPS data were calibrated according to impurity carbon 1s line (284.6 eV). Raman spectra were recorded at room temperature with microscopic confocal microscope (XploRA INV HORIBA) using a 532 nm laser beam. The contents of Pt in the precursors were determined by inductively coupled plasma atomic emission spectrometry mass spectrometry (ICP-AES, ICP-MS7700x).

2.5   Electrochemical measurements

The electrochemical measurements were conducted at room temperature (25 °C) by using the electrochemical station (CHI 760E, Shanghai Chenhua Co., China) with a three electrode system. A glassy carbon rotating disk electrode (RDE, diameter 5 mm, Pine Research Instrumentation) loaded with catalysts was served as working electrode and platinum net was used as counter electrode. A saturated calomel electrode (SCE) was used as reference electrode. All the given potentials were converted in terms of the reversible hydrogen electrode (RHE) potential. All samples were dissolved in a mixture of water, ethanol and nafion (400:400:1). The prepared catalyst slurry was dropped in the glassy carbon electrode and then was swab off by pump. The total Pt loading for each experiment were the same (6 μg). Before the electrocatalytic experiments were performed, cyclic voltammetry (CV) was conducted in N_2-saturated 0.1 M $HClO_4$ solutions in the potential region between 0.05 and 1.05 V vs. RHE at a sweep rate of 100 mV/s. The ORR performance was measured by the linear sweep voltammetry (LSV) method in O_2-saturated 0.1 M $HClO_4$ solution in the potential region between 0.05–1.05 V vs. RHE at a sweep rate of 10 mV/s. The rotation rate of RDE was 1,600 rpm in order to make the O_2 more uniform in the solution and all the polarization curves were 90% iR corrected. The current was normalized according to the electrode area (0.196 cm^2). The electrochemical surface area was determined from the hydrogen adsorption area subtracted by the double layer in the CV curve with Pt capacity of 210 μC/cm$^2_{Pt}$.

For formic acid oxidation, a three-electrode cell was also used. A glassy carbon RDE (diameter 5 mm, Pine Research Instrumentation) loaded with catalysts was served as working electrode and platinum net was used as counter electrode. A SCE was used as reference electrode. All the given potentials were converted in terms of the RHE potential. The formic acid oxidation was tested in the solution of 0.5 M H_2SO_4 + 0.25 M HCOOH at a scan rate of 100 mV/s at room temperature (25 °C). The total Pt loading for each experiment were the same (2 μg).

For methanol oxidation, a three-electrode cell was also used. A SCE was used as reference electrode. All the given potentials were converted in terms of the RHE potential. A glassy carbon RDE (diameter 5 mm, Pine Research Instrumentation) loaded with catalysts was served as working electrode and platinum net was used as counter electrode. The formic acid oxidation was tested in the solution of 0.5 M H_2SO_4 + 0.5 M CH_3OH at a scan rate of 100 mV/s at room temperature (25 °C). The total Pt loading for each experiment were the same (2 μg).

3   Results and discussion

Our proposed synthetic strategy is illustrated in Scheme 1. First, 5 nm Pt NPs capped with polyvinylpyrrolidone (PVP) were encapsulated in ZIF-8 to form rhombic dodecahedral hybrid structures (Pt@ZIF-8) (Figs. S1(a) and S1(b) in the Electronic Supplementary Material (ESM)) [38]. In the typical synthetic process, the real Pt content in the Pt@ZIF-8 precursor was ca. 10 wt.% according to ICP-MS analysis,
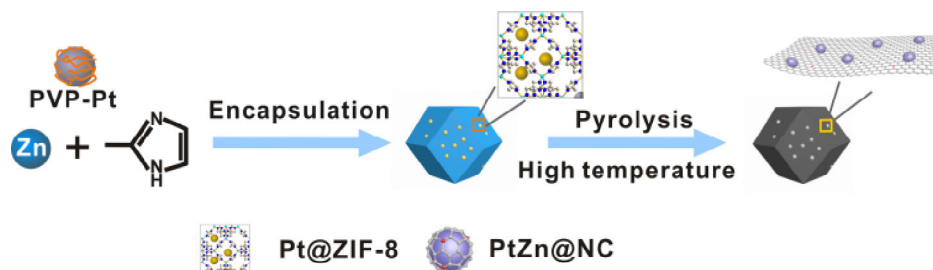
Scheme 1 Conversion of N-doped carbon shell encapsulated intermetallic PtZn NPs derived from Pt@ZIF-8 precursor via pyrolysis at high temperature.

which is in line with the raw ratio of Pt NPs relative to ZIF-8 (Table S1 in the ESM). Then, the resulting Pt@ZIF-8 precursors were heated at 200 °C for 1 h to remove guest molecules in MOF cavities and then calcined at given higher temperature (typically 800 °C) in a mix gas of H_2 and Ar (1:20) for 5 h to get intermetallic PtZn NPs supported on N-doped C matrices. For convenience, the resulting final products were denoted as 10%-PtZn@NC-X (X = 600, 700, 800, 1,000) according to the pyrolysis temperatures.

Figure 1(a) depicts the powder XRD pattern of the representative product obtained at 800 °C (i.e., 10%-PtZn@NC-800), which agrees well with the standard pattern of tetragonal intermetallic PtZn (*P4/mmm*, PDF#06-0604), without any peaks assigned to impurities. This indicates that all Pt NPs encapsulated within ZIF-8 have been alloyed with Zn atoms derived from ZIF-8 to form a ordered alloy structure via the calcination process at 800 °C. The detailed structure information of the sample 10%-PtZn@NC-800 was further provided by TEM. As shown in Fig. 1(b), the 10%-PtZn@NC-800 has lost the original rhombic dodecahedral shape of Pt@ZIF-8 precursors, indicating the pyrolysis process brought great destruction to the structure of samples. The whole particles appeared plum puddings where small metal NPs with dark contrast were separately embedded in amorphous carbon matrices. Compared to the original PVP capped Pt NPs, the average size (7 nm) of metal NPs slightly increased after calcination, which should be attributed to the lattice expansion when the evaporated Zn atoms enter the Pt NP lattices [39]. In high-resolution TEM (HRTEM) image (Fig. 1(c)), lattice fringes with 0.23 nm interplanar spacing were clearly observed on the metal NPs, which is corresponding to the {111} planes of intermetallic PtZn [39]. On the surface of PtZn NPs was covered with a thin layer of carbon, which was around 1 nm in thickness. According to previous studies [40–43], the carbon shell of 1 nm would not affect the electron transport and O_2 diffusion during ORR. Particularly, besides Pt, Zn,

and C elements, N element was also detected in 10%-PtZn@NC-800 from EDX spectroscopy analysis (Fig. S2 in the ESM). What's more, the relative atomic ratio of Zn to Pt in the sample was higher than 1:1 in intermetallic PtZn (Table S2 in the ESM).

To further confirm the composition of 10%-PtZn@NC-800 and corresponding element dispersion status, HAADF-STEM image and EDS elemental mapping were conducted (Fig. 1(d)). It was found that both N and C were homogeneously dispersed in the whole plum pudding-like particles, revealing the element N originating from the organic linker (methyl imidazole) of ZIF-8 was uniformly doped into the carbon support. The signals from the element Zn were mainly distributed in the distribution zone of Pt, but some signals were also present in the carbon support. This indicates that a small quantity of Zn atoms fell on the carbon support surface after being evaporated, which explained well the extra Zn content in the EDX analysis with regard to the sample.

Based on the above results, it can be concluded that intermetallic PtZn NPs encapsulated in N-doped carbon were successfully synthesized via our proposed method. In this synthetic process, the Pt content in Pt@ZIF-8 precursors and the pyrolysis temperature are considered two key parameters that would significantly influence the structure of the resulting PtZn@NC catalysts and their electrocatalytic performances. Given that, we conducted two series of control experiments where the Pt content in the Pt@ZIF-8 precursors or the calcination temperature were solely changed. Figure S3 in the ESM show the structure and composition of the products obtained at 800 °C by using Pt@ZIF-8 precursors of different Pt contents. It was found that metal NPs of all the samples existed in the form of intermetallic PtZn. Of note, the average sizes of as-formed intermetallic PtZn NPs were little changed at low Pt loading contents in the Pt@ZIF-8 precursors (1%, 2%, 5%, and 10%) due to the confinement effect of carbon shell. When the content of
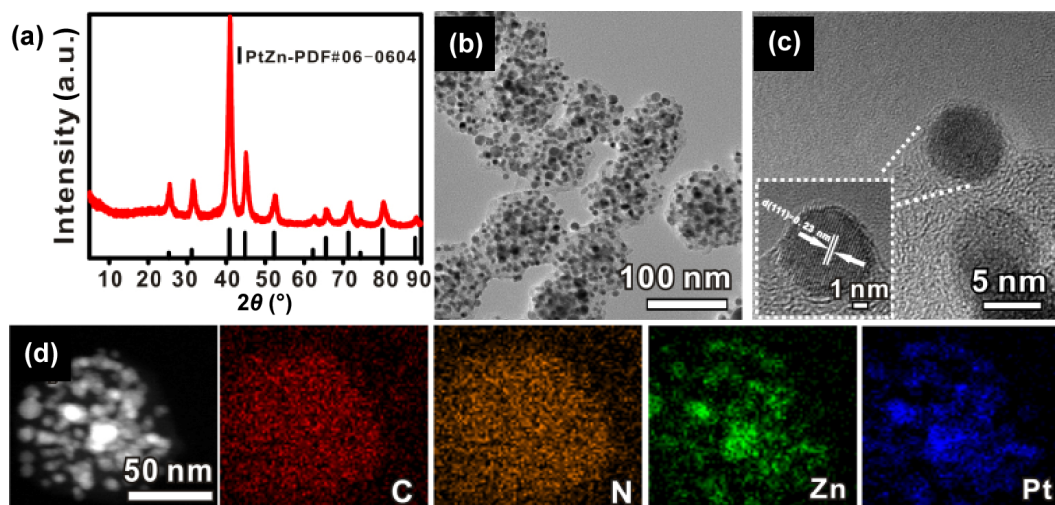

Figure 1 (a) Powder XRD pattern, (b) low magnification TEM and (c) HRTEM images of 10%-PtZn@NC-800. (d) HAADF-STEM image and EDX element mapping of 10%-PtZn@NC-800.

Pt encapsulated in ZIF-8 exceeded 10%, the average size (8.1 nm for 15% and 10.5 nm for 20%) and distribution range of PtZn NPs increased significantly. Thus it can be seen that the effect of carbon shell for inhibiting the agglomeration of metal NPs nearly failed at high Pt contents.

Next, we selected 10%-Pt@ZIF-8 as a typical precursor to study the influence of pyrolysis temperature on the structure of products. As shown in SEM images of the products obtained at different temperatures (Fig. S4 in the ESM), the shape of rhombic dodecahedron was retained for the products obtained at relatively low temperature (e.g., 600 and 700 °C), while the morphology began to be destroyed at 800 °C and completely lost at 1,000 °C. It was also found that the size distribution of metal NPs encapsulated in carbon were basically kept constant for the products obtained at 600, 700, and 800 °C, but a considerable number of larger-size metal NPs (20–45 nm) were formed when the pyrolysis temperature increased to 1,000 °C in Figs. 2(a$_1$)–2(d$_1$). This sudden change of metal NPs in size is intuitively displayed in Fig. 2(e). These results above further indicated the inhibition effect of the carbon support to the agglomeration of metal NPs. It is worth noting that the thickness of carbon shell wrapping around metal NPs gradually decreased as the pyrolysis temperature increased (Figs. 2(a$_2$)–2(d$_2$)). For example, the thickness of carbon shell was ca. 2.7 nm for the sample at 600 °C, but it decreased to ca. 1.0 nm for the sample at 800 °C. Clearly, different thicknesses of carbon shell wrapping on metal NPs would greatly affect electrocatalytic performances of the resulting PtZn@NC hybrids [40, 41].

The pyrolysis temperature also made a significant influence on the composition of metal NPs. According to the XRD analysis results in Fig. 2(f), the metal NPs in the products obtained at 600, 700, and 800 °C existed in the form of intermetallic PtZn, and the metal NPs turned into Pt rich solid solution alloy (Pt$_{rich}$Zn) of a face-centered cubic (*fcc*) structure when the pyrolysis temperature increased to 1,000 °C. This result indicates that the *fcc* structured solid solution with a disorder alloy feature is thermodynamically prone to form at higher temperature. It was also found that the Zn/Pt atomic ratios in the product significantly decreased as the temperature increased (see Table S2 in the ESM for detailed data). At relatively low temperatures (such as 600 °C), the Zn atoms reduced from ZIF-8 were hardly evaporated and thus a considerable number of Zn atoms dropped on the surface of carbon support (the atomic ratio of Zn/Pt = 4.3). The higher the temperature was; the more Zn atoms would be evaporated. The atomic ratio of Zn/Pt was close to 1:1 for the product obtained at 800 °C, and it further decreased to 0.15 for the product obtained at 1,000 °C. The XPS valence states analysis of Zn also proved such a composition change that the content of metallic Zn was relatively higher at 600 °C and decreased as the temperature increased (Fig. S5 in the ESM). In fact, it was speculated that the evaporation of more Zn atoms at high temperature facilitated the transformation from the intermetallic PtZn to the *fcc* structured Pt$_{rich}$Zn alloy.

Previous studies have demonstrated that the doping of N with high electro-negativity on C can effectively modify the electronic structure and promote the activity of ORR reaction [31–33]. In fact, the pyrolysis temperature significantly influenced the doping status of N in the carbon support. First, the N content in the products decreased as the pyrolysis temperature increased (Table S2 in the ESM). The N content was still high at 800 °C (1.37 wt.%), but it reduced severely at 1,000 °C (0.2 wt.%). As previously reported, the doping form of N in carbon is more important when the N content is sufficient [44, 45]. To confirm the existence status of N in the carbon support, high resolution XPS spectra of N 1s was conducted. As revealed in Figs. 3(a)–3(d), the N 1s spectra of the products
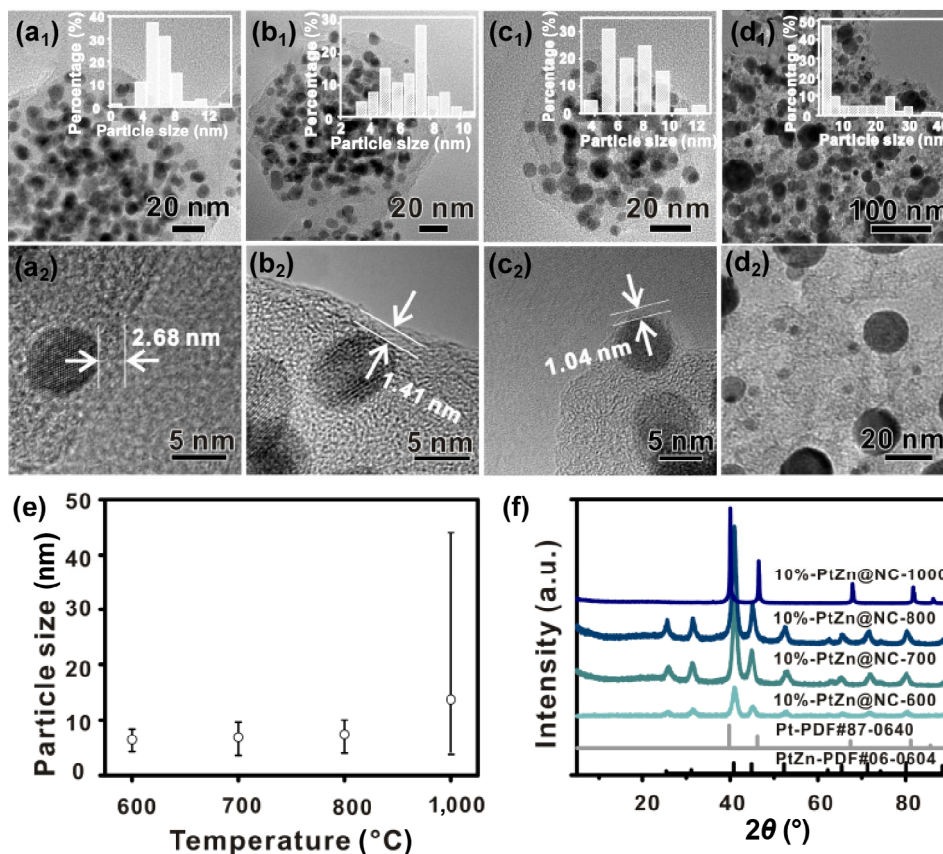

Figure 2 (a$_1$)–(d$_1$) Low magnification TEM image of PtZn@NC hybrid structure obtained at 600, 700, 800, and 1,000 °C. Insets correspond size distribution histograms of metal NPs. (a$_2$)–(d$_2$) Corresponding high magnification image of partial zones to show the covering status of carbon shell. (e) The change trend of size distributions of metal NPs in the 10%-PtZn@NC-X as a function of pyrolysis temperatures. Hollow circles represent average diameters. (f) XRD patterns of the PtZn@NC hybrid structures obtained at different temperatures.

obtained at different temperatures exhibited distinct profiles, indicating different doping status of N in the carbon support. For the 10%-PtZn@NC-600, a slightly asymmetric XPS peak of N 1s centered at 398.8 eV, which can be deconvoluted to two main kinds of N species, pyridinic N (398.3 ± 0.3 eV) and pyrrolic N (399.2 ± 0.1 eV) [46]. In the XPS spectra of N 1s for the 10%-PtZn@NC-700 and 10%-PtZn@NC-800, a shoulder peak with different intensity appeared at higher binding energy of the pyridinic N peak, which can be dominantly assigned to graphitic N (400.7 ± 0.1 eV). For the 10%-PtZn@NC-1000, the N 1s XPS peak was very weak and centered at 400.7 eV. According to the fitting with regard to XPS N 1s peaks of these samples (Fig. 3(e)), the pyrrolic and pyridinic N were dominant species in the samples obtained at low temperatures, whereas the proportion of graphitic N species gradually increased with increasing temperatures. At 1,000 °C, the element N doped in carbon support completely existed as graphitic N. Raman spectroscopy was used to examine the carbon structure in detail. As shown in Fig. 3(f), the spectrum displays intense peaks at 1,350 and 1,580 cm^{-1}, corresponding to the disordered carbon structures (D band) and the graphitized carbon (G band), respectively. The relative ratio of D to G bands (I_D/I_G) for the 10%-PtZn@NC-800 was 0.95, indicating there were a lot of defects in carbon [47]. This defect structure is usually present in N-doped graphene materials and it can produce a large number of active sites for electrocatalysis [48].

Considering the unique N-doped carbon encapsulation structure, the as-synthesized PtZn@NC hybrids are expected to exhibit excellent performances when they are applied as catalysts for fuel cells. First, the ORR activities of samples were tested using a RDE in 0.1 M HClO$_4$ solution saturated with O$_2$ at room temperature. To reveal the influence of carbon shell thickness and the metal NP size on the catalytic activities, the samples obtained at different
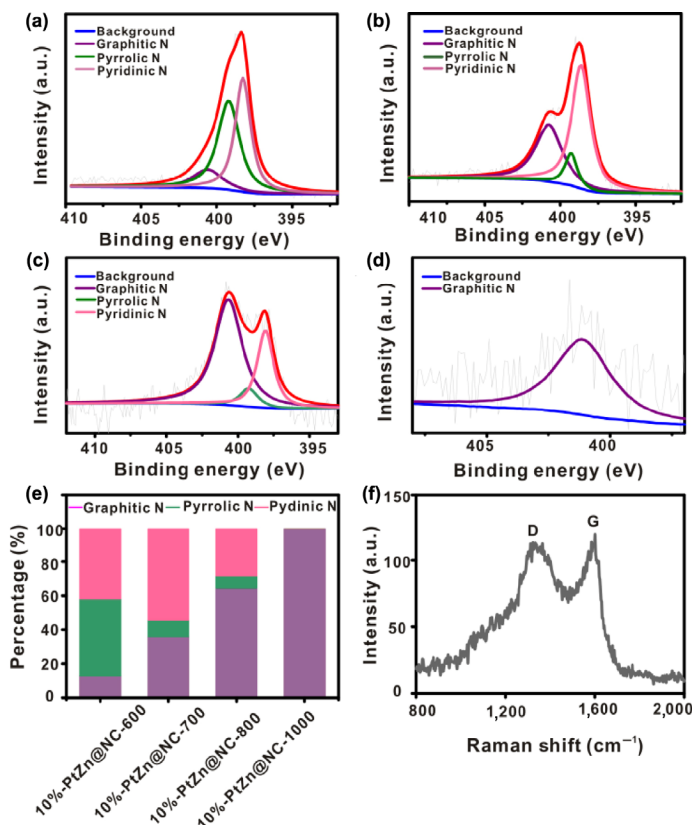
temperatures and the commercial Pt/C catalyst (20 wt.%) were measured under the same conditions. Figure 4(a) shows the ORR polarization curves on these samples. The sample 10%-PtZn@NC-600 was completely inactive for ORR in the acidic medium, and the sample 10%-PtZn@NC-1000 presented very limited activity. Clearly, the bad electrocatalytic performances of the two samples are closely related to their structures. As for the sample 10%-PtZn@NC-600, the carbon shell wrapping on the PtZn intermetallic NPs was a bit thick so that the PtZn intermetallic NPs were forfeited the catalytic activity. And for the sample 10%-PtZn@NC-1000, PtZn intermetallic NPs encapsulated in carbon grew and aggregated obviously, which severely reduced the catalyst activity. Expectedly, the two PtZn@NC samples with relatively thin carbon shells (10%-PtZn@NC-800 and 10%-PtZn@NC-700) exhibited superior activities to the commercial Pt/C. The half wave potential ($E_{1/2}$) of 10%-PtZn@NC-800 was 0.912 V, which shifted by 19 and 26 mV positively compared to the 10%-PtZn@NC-700 (0.893 V) and the commercial Pt/C catalyst (0.886 V), respectively (Table S3 in the ESM). Of note, the Tafel slope of 10%-PtZn@NC-800 (45 mV/decade) was much lower than that of commercial Pt/C (55 mV/decade), indicating more favorable catalytic kinetics on 10%-PtZn@NC-800 (Fig. S6 in the ESM). In addition, 10%-PtZn@NC-800 exhibited higher onset potential compared to commercial Pt/C (0.984 V for 10%-PtZn@NC-800, and 0.962 V for commercial Pt/C), which indicates higher intrinsic activity of 10%-PtZn@NC-800. The above results demonstrated that the thickness of the carbon layer wrapping on metal NPs is most essential for keeping catalytic activities of metal NPs [24–26]. In addition, the significantly enhanced activity for 10%-PtZn@NC-800 may result from an increase in graphitic N in carbon support. And previous studies have demonstrated that doping of graphitic N would lead to a non-uniform electron distribution, which may facilitate the adsorption of O$_2$ around Pt atoms [45, 49, 50].

The CV curves in Fig. 4(b) proved this statement. It was found that the double electric layer of 10%-PtZn@NC-800 was the smallest among all the samples, followed by the 10%-PtZn@NC-700. From the CV of 10%-PtZn@NC-600 (Fig. S7(a) in the ESM), the double electric layer of 10%-PtZn@NC-600 was very large and the current
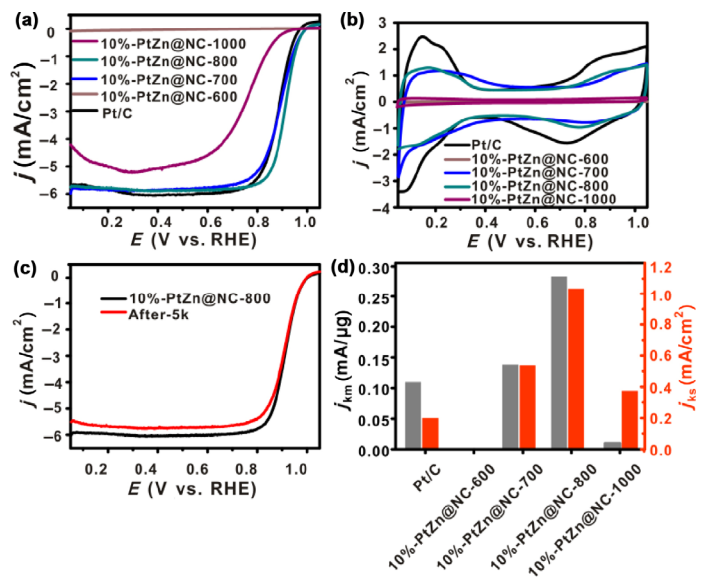

Figure 3 High resolution N 1s spectra of the products obtained at (a) 600, (b) 700, (c) 800, and (d) 1,000 °C. (e) Distribution of graphitic N, pyrrolic N and pyridinic N species in the products obtained at different temperatures. (f) Raman spectra of the product obtained at 800 °C.

Figure 4 (a) Polarization curves of the catalysts for ORR in O$_2$ saturated 0.1 M HClO$_4$ solution; scan rate, 10 mV/s; rotation rate, 1,600 rpm. Catalyst loading in terms of Pt mass: 6 μg. (b) CV curves of the products obtained at different temperatures and the commercial Pt/C in N$_2$ saturated 0.1 M HClO$_4$ solution. (c) ORR polarization curves after 5,000 CV cycles between 0.6 and 1.0 V versus RHE. Scan rate, 10 mV/s. The scan rate for the accelerated durability test (ADT) is 100 mV/s. (d) Mass activities and specific activities at 0.9 V vs. RHE.

density was very small. In addition, there was no steady-state ORR current for 10%-PtZn@NC-600, indicating no active sites exist [47]. Furthermore, it was found that almost no bare Pt existed in the 10%-PtZn@NC-600 because no hydrogen zone in CV. These results are associated with the fact the carbon layer wrapping on PtZn NPs was too thick at 600 °C. By contrast, CV of 10%-PtZn@NC-1000 revealed that there was a hydrogen zone although the current density was very small (Fig. S7(b) in the ESM).

The accelerated stress tests (ASTs) were conducted to study the catalyst stability of the best catalyst 10%-PtZn@NC-800 by cycling the potential in 0.6–1.0 V (100 mV/s) window in 0.1 M HClO$_4$ by using RDE. As shown in Fig. 4(c), the $E_{1/2}$ loss of 10%-PtZn@NC-800 was only 1 mV after 5,000 cycles. By contrast, the $E_{1/2}$ of the commercial Pt/C negatively shifted by 7 mV after 5,000 cycles, indicating its inferior stability (Fig. S8 in the ESM). TEM observation of the catalysts after ASTs indicated the PtZn nanoparticles did not increase significantly in size, and the carbon layer did not show significant corrosion. This result fully confirmed the good structure stability of as-prepared PtZn@NC hybrid catalysts (Fig. S9 in the ESM). We also compared our catalyst with other Pt-based electrocatalysts previously reported, indicating that our catalyst also has excellent stability (Table S4 in the ESM). Several key activity parameters calculated from the kinetic current density (I_k) at 0.9 V are compared in Fig. 4(d). The 10%-PtZn@NC-800 catalysts exhibited the highest mass and specific activities among the measured catalysts. The mass activity and specific activity of 10%-PtZn@NC-800 were 0.283 A/mg$_{Pt}$ and 1.03 mA/cm$_{Pt}$ at 0.9 V versus RHE in acid electrolytes, which are nearly 3 and 5 times greater that of commercial Pt/C, respectively (see Table S5 in the ESM for details).

To examine the influence of the Pt content on the activity of catalysts in ORR, we tested the samples obtained at 800 °C by using Pt@ZIF-8 precursors of different Pt contents (Fig. S10 in the ESM). It was found that the ORR activities of the catalysts as a function of their Pt contents presented a volcano shaped trend and the 10%-PtZn@NC-800 still had the highest activity among the measured samples (Table S3 in the ESM). The decreased activity of the samples with higher Pt contents (15% and 20%) should be attributed to the significant increase in sizes of PtZn intermetallic NPs. Based on the above results, it can be concluded that the catalytic activities of as-synthesized PtZn intermetallic catalyst with a N-doped carbon encapsulation structure were determined by the shell thickness and the metal NP size. To achieve optimal performances, both factors should be taken into account when designedly constructing the hybrid catalysts.

In addition to the cathodic ORR, the 10%-PtZn@NC-800 sample was applied for the anodic oxidation reaction of formic acid and methanol. Typical CVs of formic acid oxidation on the 10%-PtZn@NC-800 and commercial Pt/C were measured in a 0.5 M H$_2$SO$_4$ + 0.25 M HCOOH solution. As shown in Fig. 5(a), the 10%-PtZn@NC-800 showed a higher current density than the commercial Pt/C, with peak current density reaching 800.5 mA/mg at 0.914 V versus RHE, which is about 1.6 times as high as that of the Pt/C (see the blank columns in Fig. 5(b)). Figure 5(c) showed the CV curves for the electrocatalytic oxidation of methanol on the two catalysts in 0.5 M H$_2$SO$_4$ aqueous solution containing 0.5 M methanol. Similarly, the 10%-PtZn@NC-800 showed higher mass activity, with peak current intensity reaching 1,021 mA/mg, about 1.5 times that of the commercial Pt/C (681 mA/mg) (see the blank columns in Fig. 5(d)). The specific area activity calculated by CV (Fig. S11 in the ESM) is listed in Table S6 in the ESM. In fact, even with normalized by their electrochemically active surface area (ECSA), the catalytic activity of the 10%-PtZn@NC-800 was still higher than that of Pt/C (Fig. 5(d)). The specific activity of 10%-PtZn@NC-800 was 3 and 3.5 times that of the commercial Pt/C in the electrocatalytic oxidation of methanol and formic acid. In
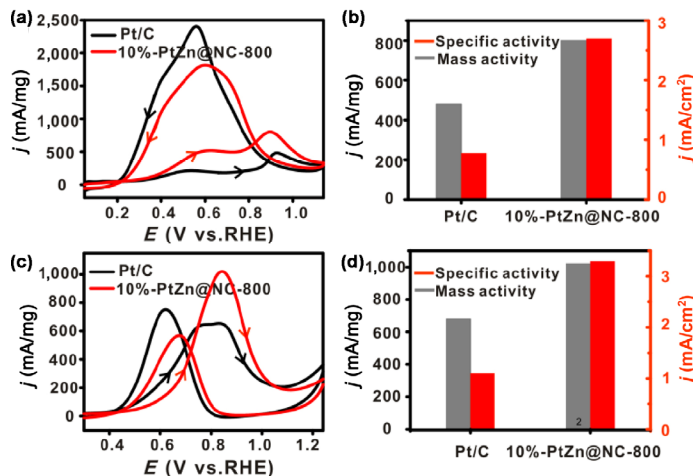

Figure 5 (a) Formic acid oxidation in an 0.5 M H$_2$SO$_4$ + 0.25 M HCOOH solution (scan rate, 100 mV/s). (b) Mass activity and specific area activity for formic acid oxidation. (c) Methanol oxidation in an 0.5 M H$_2$SO$_4$ + 0.5 M CH$_3$OH solution (scan rate, 100 mV/s). (d) Mass activity and specific area activity for methanol oxidation.

addition, chronoamperometric curves showed that the current density on 10%-PtZn@NC-800 was still much higher than that on commercial Pt/C after 1,000 s in both tests, which indicates the better stability of 10%-PtZn@NC-800 (Fig. S12 in the ESM). As we know, conventional Pt catalysts are readily self-poisoned by the CO that is produced as a byproduct in the electrocatalytic oxidation of formic acid and methanol. Clearly, the as-prepared 10%-PtZn@NC-800 is less susceptible to CO poisoning due to the formation of intermetallic PtZn and the carbon shell encapsulation structure [7, 14, 21, 51]. To confirm this, CO-stripping experiments were further conducted. It was found that the CO oxidation potential of 10%-PtZn@NC-800 was 36 mV forward compared to the commercial Pt-C, indicating that it has excellent resistance to CO oxidation (Fig. S13 in the ESM).

4 Conclusion

In summary, we successfully fabricated a highly active multifunctional ordered PtZn intermetallic NPs embedded inside N-doped carbon by one step pyrolysis of Pt-incorporated ZIF-8. N-doped carbon encapsulated PtZn intermetallic NPs achieved significantly enhanced activity for the ORR in acidic media compared to the commercial Pt/C. The best sample 10%-PtZn@NC-800 exhibited a half wave potential ($E_{1/2}$) of 0.912 V, which positively shifted by 26 mV compared to the commercial Pt/C catalyst (0.886 V). Furthermore, the sample showed significantly enhanced electro-catalytic performances towards methanol oxidation and formic acid oxidation. The outstanding performance of the sample is attributed to the synergistic effects of a high degree of graphitic N species, the carbon shell encapsulation structure, and the unique geometric and electronic structure of intermetallic PtZn NPs. Specifically, we found that the thickness of carbon shell in this encapsulated catalyst is very crucial for the full exertion of the above synergistic effects. Therefore this work well demonstrated that ideal hybrid catalysts with desirable activity and stability could be produced by rationally engineering the interface structure between active metal NPs and carbon supports.

References

[1] Gasteiger, H. A.; Kocha, S. S.; Sompalli, B.; Wagner, F. T. Activity benchmarks and requirements for Pt, Pt-alloy, and non-Pt oxygen reduction catalysts for PEMFCs. *Appl. Catal. B*: *Environ*. **2005**, *56*, 9–35.

[2] Yu, X. W.; Ye, S. Y. Recent advances in activity and durability enhancement of Pt/C catalytic cathode in PEMFC: Part I. Physico-chemical and electronic interaction between Pt and carbon support, and activity enhancement of Pt/C catalyst. *J. Power Sources* **2007**, *172*, 133–144.

[3] Sopian, K.; Wan Daud, W. R. Challenges and future developments in proton exchange membrane fuel cells. *Renew. Energy* **2006**, *31*, 719–727.

[4] Li, M. F.; Zhao, Z. P.; Cheng, T.; Fortunelli, A.; Chen, C. Y.; Yu, R.; Zhang, Q. H.; Gu, L.; Merinov, B. V.; Lin, Z. Y. et al. Ultrafine jagged platinum nanowires enable ultrahigh mass activity for the oxygen reduction reaction. *Science* **2016**, *354*, 1414–1419.

[5] Stamenkovic, V. R.; Fowler, B.; Mun, B. S.; Wang, G. F.; Ross, P. N.; Lucas, C. A.; Marković, N. M. Improved oxygen reduction activity on $Pt_3Ni(111)$ via increased surface site availability. *Science* **2007**, *315*, 493–497.

[6] Sasaki, K.; Naohara, H.; Choi, Y.; Cai, Y.; Chen, W. F.; Liu, P.; Adzic, R. R. Highly stable Pt monolayer on PdAu nanoparticle electrocatalysts for the oxygen reduction reaction. *Nat. Commun*. **2012**, *3*, 1115.

[7] Qi, Z. Y.; Xiao, C. X.; Liu, C.; Goh, T. W.; Zhou, L.; Maligal-Ganesh, R.; Pei, Y. C.; Li, X. L.; Curtiss, L. A.; Huang, W. Y. Sub-4 nm PtZn intermetallic nanoparticles for enhanced mass and specific activities in catalytic electrooxidation reaction. *J. Am. Chem. Soc*. **2017**, *139*, 4762–4768.

[8] Zhu, J.; Zheng, X.; Wang, J.; Wu, Z. X.; Han, L. L.; Lin, R. Q.; Xin, H. L.; Wang, D. L. Structurally ordered Pt–Zn/C series nanoparticles as efficient anode catalysts for formic acid electrooxidation. *J. Mater. Chem. A* **2015**, *3*, 22129–22135.

[9] Porter, N. S.; Wu, H.; Quan, Z. W.; Fang, J. Y. Shape-control and electrocatalytic activity-enhancement of Pt-based bimetallic nanocrystals. *Acc. Chem. Res*. **2013**, *46*, 1867–1877.

[10] Wang, Y. J.; Zhao, N. N.; Fang, B. Z.; Li, H.; Bi, X. T.; Wang, H. J. Carbon-supported Pt-based alloy electrocatalysts for the oxygen reduction reaction in polymer electrolyte membrane fuel cells: Particle size, shape, and composition manipulation and their impact to activity. *Chem. Rev*. **2015**, *115*, 3433–3467.

[11] Chen, Q. L.; Cao, Z. M.; Du, G. F.; Kuang, Q.; Huang, J.; Xie, Z. X.; Zheng, L. S. Excavated octahedral Pt-Co alloy nanocrystals built with ultrathin nanosheets as superior multifunctional electrocatalysts for energy conversion applications. *Nano Energy* **2017**, *39*, 582–589.

[12] Huang, Y.; Garcia, M.; Habib, S.; Shui, J. L.; Wagner, F. T.; Zhang, J. L.; Jorné, J.; Li, J. C. M. Dealloyed PtCo hollow nanowires with ultrathin wall thicknesses and their catalytic durability for the oxygen reduction reaction. *J. Mater. Chem. A* **2014**, *2*, 16175–16180.

[13] Zhu, Z. J.; Zhai, Y. L.; Dong, S. J. Facial synthesis of PtM (M = Fe, Co, Cu, Ni) bimetallic alloy nanosponges and their enhanced catalysis for oxygen reduction reaction. *ACS Appl. Mater. Interfaces* **2014**, *6*, 16721–16726.

[14] Chen, Q. L.; Zhang, J. W.; Jia, Y. Y.; Jiang, Z. Y.; Xie, Z. X.; Zheng, L. S. Wet chemical synthesis of intermetallic Pt_3Zn nanocrystals via weak reduction reaction together with upd process and their excellent electrocatalytic performances. *Nanoscale* **2014**, *6*, 7019–7024.

[15] Gan, L.; Rudi, S.; Cui, C. H.; Heggen, M.; Strasser, P. Size-controlled synthesis of sub-10 nm $PtNi_3$ alloy nanoparticles and their unusual volcano-shaped size effect on orr electrocatalysis. *Small* **2016**, *12*, 3189–3196.

[16] Chen, C.; Kang, Y. J.; Huo, Z. Y.; Zhu, Z. W.; Huang, W. Y.; Xin, H. L.; Snyder, J. D.; Li, D. G.; Herron, J. A.; Mavrikakis, M. et al. Highly crystalline multimetallic nanoframes with three-dimensional electrocatalytic surfaces. *Science* **2014**, *343*, 1339–1343.

[17] Bu, L. Z.; Zhang, N.; Guo, S. J.; Zhang, X.; Li, J.; Yao, J. L.; Wu, T.; Lu, G.; Ma, J. Y.; Su, D. et al. Biaxially strained PtPb/Pt core/shell nanoplate boosts oxygen reduction catalysis. *Science* **2016**, *354*, 1410–1414.

[18] Taniguchi, A.; Akita, T.; Yasuda, K.; Miyazaki, Y. Analysis of electrocatalyst degradation in PEMFC caused by cell reversal during fuel starvation. *J. Power Sources* **2004**, *130*, 42–49.

[19] Iihama, S.; Furukawa, S.; Komatsu, T. Efficient catalytic system for chemoselective hydrogenation of halonitrobenzene to haloaniline using PtZn intermetallic compound. *ACS Catal*. **2016**, *6*, 742–746.

[20] Wang, W.; Lei, B.; Guo, S. J. Engineering multimetallic nanocrystals for highly efficient oxygen reduction catalysts. *Adv. Energy Mater*. **2016**, *6*, 1600236.

[21] Ji, X. L.; Lee, K. T.; Holden, R.; Zhang, L.; Zhang, J. J.; Botton, G. A.; Couillard, M.; Nazar, L. F. Nanocrystalline intermetallics on mesoporous carbon for direct formic acid fuel cell anodes. *Nat. Chem*. **2010**, *2*, 286–293.

[22] Wang, J.; Wu, H. H.; Gao, D. F.; Miao, S.; Wang, G. X.; Bao, X. H. High-density iron nanoparticles encapsulated within nitrogen-doped carbon nanoshell as efficient oxygen electrocatalyst for zinc–air battery. *Nano Energy* **2015**, *13*, 387–396.

[23] Deng, J.; Ren, P. J.; Deng, D. H.; Yu, L.; Yang, F.; Bao, X. H. Highly active and durable non-precious-metal catalysts encapsulated in carbon nanotubes for hydrogen evolution reaction. *Energy Environ. Sci*. **2014**, *7*, 1919–1923.

[24] Chen, X. Q.; Yu, L.; Wang, S. H.; Deng, D. H.; Bao, X. H. Highly active and stable single iron site confined in graphene nanosheets for oxygen reduction reaction. *Nano Energy* **2017**, *32*, 353–358.

[25] Li, H. B.; Xiao, J. P.; Fu, Q.; Bao, X. H. Confined catalysis under two-dimensional materials. *Proc. Natl. Acad. Sci. USA* **2017**, *114*, 5930–5934.

[26] Deng, J.; Deng, D. H.; Bao, X. H. Robust catalysis on 2D materials encapsulating metals: Concept, application, and perspective. *Adv. Mater*. **2017**, *29*, 1606967.

[27] Cui, T. T.; Dong, J. H.; Pan, X. L.; Yu, T.; Fu, Q.; Bao, X. H. Enhanced hydrogen evolution reaction over molybdenum carbide nanoparticles confined inside single-walled carbon nanotubes. *J. Energy Chem*. **2019**, *28*, 123–127.

[28] Xiao, M. L.; Zhu, J. B.; Feng, L. G.; Liu, C. P.; Xing, W. Meso/macroporous nitrogen-doped carbon architectures with iron carbide encapsulated in graphitic layers as an efficient and robust catalyst for the oxygen reduction reaction in both acidic and alkaline solutions. *Adv. Mater*. **2015**, *27*, 2521–2527.

[29] Cui, X. J.; Ren, P. J.; Deng, D. H.; Deng, J.; Bao, X. H. Single layer graphene encapsulating non-precious metals as high-performance electrocatalysts for water oxidation. *Energy Environ. Sci*. **2016**, *9*, 123–129.

[30] Deng, J.; Ren, P. J.; Deng, D. H.; Bao, X. H. Enhanced electron penetration through an ultrathin graphene layer for highly efficient catalysis of the hydrogen evolution reaction. *Angew. Chem., Int. Ed*. **2015**, *54*, 2100–2104.

[31] Zhao, Z. H.; Li, M. T.; Zhang, L. P.; Dai, L. M.; Xia, Z. H. Design principles for heteroatom-doped carbon nanomaterials as highly efficient catalysts for fuel cells and metal-air batteries. *Adv. Mater*. **2015**, *27*, 6834–6840.

[32] Du, N. N.; Wang, C. M.; Long, R.; Xiong, Y. J. N-doped carbon-stabilized PtCo nanoparticles derived from Pt@ZIF-67: Highly active and durable catalysts for oxygen reduction reaction. *Nano Res*. **2017**, *10*, 3228–3237.

[33] Wang, X. X.; Hwang, S.; Pan, Y. T.; Chen, K.; He, Y. H.; Karakalos, S.; Zhang, H. G.; Spendelow, J. S.; Su, D.; Wu, G. Ordered Pt_3Co intermetallic nanoparticles derived from metal-organic frameworks for oxygen reduction. *Nano Lett*. **2018**, *18*, 4163–4171.

[34] Chen, Y. Z.; Wang, C. M.; Wu, Z. Y.; Xiong, Y. J.; Xu, Q.; Yu, S. H.; Jiang, H. L. From bimetallic metal-organic framework to porous carbon: High surface area and multicomponent active dopants for excellent electrocatalysis. *Adv. Mater*. **2015**, *27*, 5010–5016.

[35] Li, F. L.; Shao, Q.; Huang, X. Q.; Lang, J. P. Nanoscale trimetallic metal-organic frameworks enable efficient oxygen evolution electrocatalysis. *Angew. Chem., Int. Ed*. **2018**, *57*, 1888–1892.

[36] Shao, Q.; Yang, J.; Huang, X. Q. The design of water oxidation electrocatalysts from nanoscale metal-organic frameworks. *Chem.—Eur. J*. **2018**, *24*, 15143–15155.

[37] Zhang, N.; Shao, Q.; Wang, P. T.; Zhu, X.; Huang, X. Q. Porous Pt-Ni nanowires within *in situ* generated metal-organic frameworks for highly chemoselective cinnamaldehyde hydrogenation. *Small* **2018**, *14*, e1704318.

[38] Lu, G.; Li, S. Z.; Guo, Z.; Farha, O. K.; Hauser, B. G.; Qi, X. Y.; Wang, Y.; Wang, X.; Han, S. Y.; Liu, X. G. et al. Imparting functionality to a metal-organic framework material by controlled nanoparticle encapsulation. *Nat. Chem*. **2012**, *4*, 310–316.

[39] Qi, Z. Y.; Pei, Y. C.; Goh, T. W.; Wang, Z. Y.; Li, X. L.; Lowe, M.; Maligal-Ganesh, R. V.; Huang, W. Y. Conversion of confined metal@ZIF-8 structures to intermetallic nanoparticles supported on nitrogen-doped carbon for electrocatalysis. *Nano Res*. **2018**, *11*, 3469–3479.

[40] Deng, J.; Yu, L.; Deng, D. H.; Chen, X. Q.; Yang, F.; Bao, X. H. Highly active reduction of oxygen on a FeCo alloy catalyst encapsulated in pod-like carbon nanotubes with fewer walls. *J. Mater. Chem. A* **2013**, *1*, 14868–14873.

[41] Guinea, F. Charge distribution and screening in layered graphene systems. *Phys. Rev. B* **2007**, *75*, 235433.

[42] Chen, H. A.; Hsin, C. L.; Huang, Y. T.; Tang, M. L.; Dhuey, S.; Cabrini, S.; Wu, W. W.; Leone, S. R. Measurement of interlayer screening length of layered graphene by plasmonic nanostructure resonances. *J. Phys. Chem. C* **2013**, *117*, 22211–22217.

[43] Deng, D. H.; Yu, L.; Chen, X. Q.; Wang, G. X.; Jin, L.; Pan, X. L.; Deng, J.; Sun, G. Q.; Bao, X. H. Iron encapsulated within pod-like carbon nanotubes for oxygen reduction reaction. *Angew. Chem., Int. Ed.* **2013**, *52*, 371–375.

[44] Wu, G.; Mack, N. H.; Gao, W.; Ma, S. G.; Zhong, R. Q.; Han, J. T.; Baldwin, J. K.; Zelenay, P. Nitrogen-doped graphene-rich catalysts derived from heteroatom polymers for oxygen reduction in nonaqueous lithium-O$_2$ battery cathodes. *ACS Nano* **2012**, *6*, 9764–9776.

[45] Li, Q.; Xu, P.; Gao, W.; Ma, S. G.; Zhang, G. Q.; Cao, R. G.; Cho, J.; Wang, H. L.; Wu, G. Graphene/graphene-tube nanocomposites templated from cage-containing metal-organic frameworks for oxygen reduction in li-O$_2$ batteries. *Adv. Mater.* **2014**, *26*, 1378–1386.

[46] Zheng, F. C.; Yang, Y.; Chen, Q. W. High lithium anodic performance of highly nitrogen-doped porous carbon prepared from a metal-organic framework. *Nat. Commun.* **2014**, *5*, 5261.

[47] Zhu, Y. W.; Murali, S.; Cai, W. W.; Li, X. S.; Suk, J. W.; Potts, J. R.; Ruoff, R. S. Graphene and graphene oxide: Synthesis, properties, and applications. *Adv. Mater.* **2010**, *22*, 3906–3924.

[48] Shi, P. C.; Yi, J. D.; Liu, T. T.; Li, L.; Zhang, L. J.; Sun, C. F.; Wang, Y. B.; Huang, Y. B.; Cao, R. Hierarchically porous nitrogen-doped carbon nanotubes derived from core–shell ZnO@zeolitic imidazolate framework nanorods for highly efficient oxygen reduction reactions. *J. Mater. Chem. A* **2017**, *5*, 12322–12329.

[49] Sidik, R. A.; Anderson, A. B.; Subramanian, N. P.; Kumaraguru, S. P.; Popov, B. N. O$_2$ reduction on graphite and nitrogen-doped graphite: Experiment and theory. *J. Phys. Chem. B* **2006**, *110*, 1787–1793.

[50] Zhang, H. G.; Hwang, S.; Wang, M. Y.; Feng, Z. X.; Karakalos, S.; Luo, L. L.; Qiao, Z.; Xie, X. H.; Wang, C. M.; Su, D. et al. Single atomic iron catalysts for oxygen reduction in acidic media: Particle size control and thermal activation. *J. Am. Chem. Soc.* **2017**, *139*, 14143–14149.

[51] Miura, A.; Wang, H. S.; Leonard, B. M.; Abruña, H. D.; DiSalvo, F. J. Synthesis of intermetallic PtZn nanoparticles by reaction of Pt nanoparticles with Zn vapor and their application as fuel cell catalysts. *Chem. Mater.* **2009**, *21*, 2661–2667.